Front. Optoelectron. 2019, 12(4): 352–364
https://doi.org/10.1007/s12200-019-0907-4

RESEARCH ARTICLE

Antimony doped Cs_2SnCl_6 with bright and stable emission

Jinghui LI[1,*], Zhifang TAN[1,2,*], Manchen HU[1], Chao CHEN[1,2], Jiajun LUO[1], Shunran LI[1], Liang GAO[1], Zewen XIAO[1], Guangda NIU (✉)[1], Jiang TANG (✉)[1,2]

1 Wuhan National Laboratory for Optoelectronics (WNLO), Huazhong University of Science and Technology, Wuhan 430074, China
2 School of Optical and Electronic Information, Huazhong University of Science and Technology, Wuhan 430074, China

Abstract Lead halide perovskites, with high photoluminescence efficiency and narrow-band emission, are promising materials for display and lighting. However, the lead toxicity and environmental sensitivity hinder their potential applications. Herein, a new antimony-doped lead-free inorganic perovskites variant Cs_2SnCl_6:*x*Sb is designed and synthesized. The perovskite variant Cs_2SnCl_6:*x*Sb exhibits a broadband orange-red emission, with a photoluminescence quantum yield (PLQY) of 37%. The photoluminescence of Cs_2SnCl_6:*x*Sb is caused by the ionoluminescence of Sb^{3+} within Cs_2SnCl_6 matrix, which is verified by temperature dependent photoluminescence (PL) and PL decay measurements. In addition, the all inorganic structure renders Cs_2SnCl_6:*x*Sb with excellent thermal and water stability. Finally, a white light-emitting diode (white-LED) is fabricated by assembling Cs_2SnCl_6:0.59%Sb, Cs_2SnCl_6:2.75%Bi and $Ba_2Sr_2SiO_4$:Eu^{2+} onto the commercial UV LED chips, and the color rendering index (CRI) reaches 81.

Keywords perovskite, lead-free, antimony doping, orange-red emission

1 Introduction

Lead halide perovskites have attracted tremendous research interests due to their excellent performance in photovoltaic, electroluminescence, bio imaging, display etc. [1–7]. In terms of light emitting applications, the performances of lead halide perovskite light-emitting diodes (PeLEDs) have been improved dramatically to over 20% of external quantum efficiency in a short period [8–10]. Lead halide perovskites have also exhibited many other favorable advantages such as high photoluminescence quantum yield (PLQY) ($>95\%$), narrow full width at half maximum (FWHM <20 nm), low-cost solution synthesis [11,12]. Besides, by adjusting the type and proportion of halogens, the emission spectrum of lead halide perovskites can cover the entire visible spectrum and the color gamut could even reach 140% of National Television Standards Committee (NTSC) color standards [13,14]. However, lead halide perovskites contain poisonous Pb element, which not only damages humans' nervous system but also ruins local ecosystems [15]. Moreover, the poor stability of lead halide perovskites is another annoying disadvantage, such as the high susceptibility toward moisture and thermal treatment etc [16–18]. Hence, developing perovskites or perovskite variants, with non-toxic compositions and good stability is a key step toward practical applications.

Several lead-free halide perovskites have been reported, such as $CsSnX_3$ (X = Cl, Br, I), $MA_3Bi_2X_9$ and $Cs_3Sb_2X_9$, etc. [19–22]. These materials have barely exhibited satisfactory photoluminescence and stability. By tuning the crystal structure and reducing the electronic dimensionality, Ma and coworkers reported a series of luminescent lead-free perovskite variants via the use of long chain amines for dimensionality reduction, such as (1-butyl-1-methylpyrrolidinium (C_9NH_{20}))$_2SbCl_5$ and (Tetraphenylphosphonium (Ph_4P))$_2SbCl_5$ [23,24]. The stability against water and heat however needs to be further improved due to the presence of organic amines. Recent studies have demonstrated the use of doping as another effective method to tune the photoluminescence properties, like Mn^{2+} or rare earth ion doped lead halide perovskites [25–27]. The strong exciton confinement in ion luminescent center, similar with dimensionality reduction in essence, is also beneficial for photoluminescence. Dopant emission is relatively less explored, particularly in an inorganic perovskite structure which enjoys the good stability toward

Received February 14, 2019; accepted March 16, 2019

E-mails: guangda_niu@hust.edu.cn, jtang@mail.hust.edu.cn

*These authors contributed equally.

external conditions. It is thus scientifically interesting to explore more doping ions in lead-free perovskites and produce multi-colored emissions for potential lighting and display applications.

Herein we introduced antimony cations (Sb^{3+}) into Cs_2SnCl_6, the previously established matrix material [28], to obtain a new phosphor with a broadband orange-red emission (peak position at 602 nm; FWHM ~101 nm). By introducing Sb^{3+} into the vacancy-ordered double perovskite Cs_2SnCl_6, a significant boost of PLQY (~37%) was observed compared to the non-luminescent Cs_2SnCl_6. The stability against water and heat of Sb^{3+} doped Cs_2SnCl_6 is superior among halide perovskites due to its all-inorganic structure. At last, we demonstrated a white light-emitting diode (white-LED) by assembling Cs_2SnCl_6:0.59%Sb, Cs_2SnCl_6:2.75%Bi and $Ba_2Sr_2SiO_4:Eu^{2+}$ onto the commercial UV LED chips, and the color rendering index (CRI) reaches 81. The high stability and CRI endow this all-inorganic lead-free material with highly promising prospects in lighting application.

2 Experimental section

Materials and Chemicals: Cesium chloride (CsCl, 99.99%), tin chloride ($SnCl_2$, 99.999%) and antimony (III) oxide (Sb_2O_3, 99.9%) were purchased from Alfa Aesar. Hydrochloric acid (HCl, 37wt% in water) was purchased from Sinopharm Chemical Reagent Co., Ltd, China. All materials and chemicals were used without further purification, unless otherwise noted.

Growth of Cs_2SnCl_6:xSb crystals: Cs_2SnCl_6:*x*Sb crystals were grown from HCl solution by hydrothermal method. 336.72 mg (2 mmol) CsCl, 189.60 mg (1 mmol) $SnCl_2$, and 1.458 – 43.73 mg (0.01 – 0.3 mmol) Sb_2O_3 and 4 mL HCl were loaded into a poly(tetrafluoroethylene) container successively. The container was placed in a hydrothermal autoclave and heated to 180°C for dissolving the raw materials completely. Crystals were obtained by slowly cooling the solution down to room temperature over the course of 20 h. The obtained crystals of Cs_2SnCl_6:xSb^{3+} were rinsed with methanol three times to remove the surface impurity, dried naturally and then collected for further analysis.

Fabrication of white-LED devices: White-LED was fabricated by using a UV LED chips (EPILEDS, 380 nm) to excite the phosphor-silicone mixture. The mixture was obtained after gelling in air naturally by mixing Cs_2SnCl_6:xSb^{3+}, Cs_2SnCl_6:xBi^{3+}, commercial green phosphors ($GaAlSiN_3:Eu^{2+}$) and tetraethyl orthosilicate (TEOS) with the addition of proper amount of water and HBr to promote the hydrolysis of TEOS. The UV LEDs were driven by a Keithley 2400 source meter and emission spectra were recorded on a PR655 Portable spectrophotometer.

Structural characterization: The X-ray diffraction (XRD) experiments were performed by powder X-ray diffraction (PXRD) (D8 ADVANCE, Bruker, using a Cu Kα rotating anode). The surface of Cs_2SnCl_6:*x*Sb crystals were analyzed using XPS with Al Kα excitation (Genesis, EDAX Inc., 300 W). Thermogravimetric analysis (TGA) results were obtained using a PerkinElmer Diamond TG/DTA6300, while the Cs_2SnCl_6:0.59%Sb crystals were heated from room temperature (around 20°C) to 700°C at a rate of 10°C min^{-1} in N_2 flow within an alumina crucible.

Optical characterization: UV-Vis absorption spectra were measured with powder samples. PLQY, steady-state and time-resolved photoluminescence (TRPL) spectra were recorded on an Edinburgh Instruments FLS980 spectrometer with a red-sensitive photomultiplier tube (R928), equipped with a xenon lamp and a time-correlated single photon counting (TCSPC) module (diode laser excitation at λ = 375 nm) and an integrating sphere. The temperature-dependent photoluminescence (PL) spectra were measured with a temperature controller system. The spectra were corrected for the monochromator wavelength dependence and photomultiplier response functions provided by the manufacturer. The measurements were performed using dried, powdered polycrystalline samples. No filters were used during the TRPL measurement.

3 Results and discussion

Sb^{3+}-doped Cs_2SnCl_6 crystals were synthesized through the conventional hydrothermal method. In detail, cesium chloride (CsCl), tin chloride ($SnCl_2$) and antimony oxide (Sb_2O_3) were added into HCl aqueous solution in a PTFE container of hydrothermal reactors. Then the solution was kept at 180°C for 10 h to ensure the complete dissolution of all precursors. After a slow cooling down process from 180°C to room temperature for 20 h, tiny crystals could be formed in the solution. To ensure the total removal of surface-adsorbed ions, the tiny crystals were rinsed by methanol for three times. The Sb/(Sb + Sn) molar ratios in the solution were set at 0, 0.99%, 4.76%, 9.09%, 16.66% and 23.08%. The whole procedure was conducted in air atmosphere. Here we utilized Sb_2O_3 instead of $SbCl_3$ as Sb^{3+} precursors due to the high hygroscopicity of $SbCl_3$ and hence the difficulty in accurate weighing. The reason why we chose Sn (II) as the tin source will be discussed in the later part of the calculation for chemical potential ($\Delta\mu$) and formation enthalpies (ΔH). X-ray diffraction (XRD) measurement was applied to determine the structure of the samples and the result is shown in Fig. 1(a). Without any impurity phase, all the diffraction peaks of products matched well with Cs_2SnCl_6 crystal structure (ISCD #9023) with a space group of $Fm\bar{3}m$. Inductively coupled plasma optical emission spectrometry (ICP-OES) was used to precisely determine the chemical compositions of

products. As shown in Table S1, the ICP-OES-determined Sb/(Sb + Sn) concentrations are 0.20%, 0.41%, 0.59%, 0.89% and 0.98%, while the feeding concentrations are 0.99%, 4.76%, 9.09%, 16.66% and 23.08%, respectively. To simplify later discussion, we label the samples as Cs_2SnCl_6:*x*Sb, where *x* is the real concentration provided by ICP-OES. It should be noted that the Sb concentrations are fairly low compared to the Bi concentrations reported in our previous work [28]. X-ray photoelectron spectroscopy (XPS) measurement was utilized to further verify the composition and obtain the valence state of the elements within the products. The XPS survey spectrum (Fig. 1(b)) shows the characteristic peaks for Cs, Sn, Cl and Sb. As shown in Fig. S2(a), the peaks locating at 496.3 and 487.8 eV correspond to Sn^{4+} 3d3/2 and 3d5/2, respectively, proving that the Sn^{2+} was completely oxidized to Sn^{4+} after the reaction process in the hydrothermal reactor. The peaks locating at 540.0 and 532.9 eV correspond to Sb^{3+} 3d3/2 and 3d5/2, respectively (Fig. S2(b)). There is an additional peak at 531.7eV in Fig. S2(b), which was tentatively attributed to the presence of Sb-O or Sn-O on the crystal surface due to the hydrolysis of antimony chloride and tin chloride [29–32]. From the XRD, ICP-OES and XPS measurements, we speculate that the Sb^{3+} was incorporated into the Cs_2SnCl_6 matrix successfully. Moreover, the chemical potential window and formation enthalpies for Sb interstitial (Sb_i) and Sb-Sn substitution (Sb_{Sn}) were calculated (Figs. 1(c) and 1(d)). The $\Delta H > 0$ means that it is not conducive to forming such products. Hence the results reveal that Sb_i can hardly form because of the too high ΔH values in the whole chemical potential regions, and Sb_{Sn} can also hardly form under Sn^{4+}-rich/Sn^{2+}-poor conditions (i.e., in the high $\Delta\mu_{sn}$ regions C-F in Fig. 1(c)). Instead, the use of Sn^{4+}-poor/Sn^{2+}-rich condition (i.e., in the low $\Delta\mu_{sn}$ regions A, B, and G) is favorable for the formation of Sb_{Sn}, where the ΔH values are low or even negative. Thereby we chose Sn (II) as the tin source for the synthesis of antimony ion doped Cs_2SnCl_6, in analogy with our previous synthesis of Cs_2SnCl_6:*x*Bi. The refined lattice parameters of Cs_2SnCl_6:*x*Sb samples increased as the Sb concentration increased (see Fig. S1 and Table S2 in the Supporting Information),

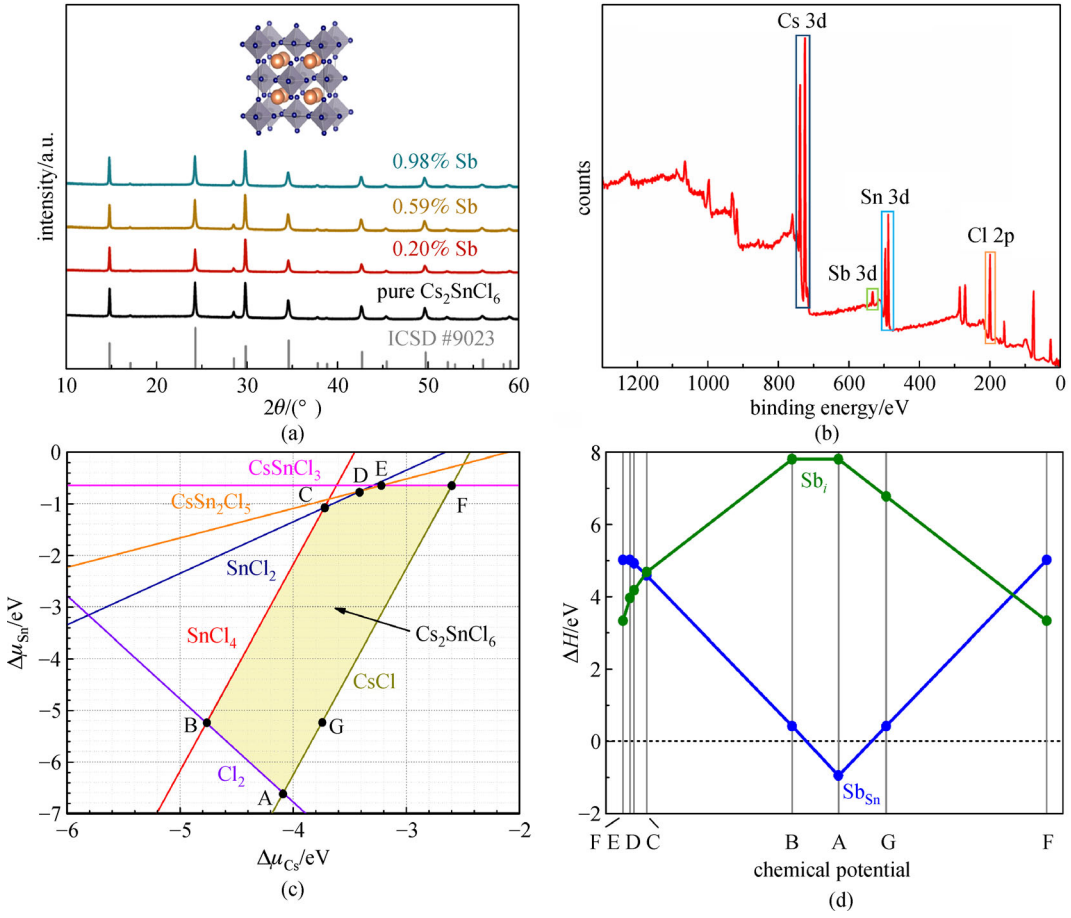

Fig. 1 (a) XRD patterns of Cs_2SnCl_6:*x*Sb powders with representative Sb content. The inset is the crystal structure of vacancy ordered double perovskite Cs_2SnCl_6. Dark purple spheres: Cl; tawny spheres: Cs; gray spheres: Sn. (b) XPS survey spectrum for Cs_2SnCl_6:0.59% Sb. (c) Calculated polyhedron of the chemical potential region where Cs_2SnCl_6 is stable against possible competitive phases. (d) Calculated formation enthalpies (ΔH) of neutral Sb_i and Sb_{Sn} as a function of the chemical potentials ($\Delta\mu_{Cs}$, $\Delta\mu_{Sn}$), where ($\Delta\mu_{Cs}$, $\Delta\mu_{Sn}$) moves along the F-E-D-C-B-A-G-F lines in (c)

which is consistent with ion radius of Sn^{4+} (0.69 Å) and Sb^{3+} (0.76 Å) for Sb-Sn substitution.

Then the PL properties of Cs_2SnCl_6:*x*Sb were studied by steady-state and TRPL spectroscopy. Sb-doped Cs_2SnCl_6 samples exhibited a broadband orange photoluminescence under 365 nm UV excitation (inset of Fig. 2(a)), while Cs_2SnCl_6 exhibited no photoluminescence. The results were summarized in Table 1, and Cs_2SnCl_6:*x*Sb with various doping concentrations exhibited similar emission and excitation spectra. PLQY was directly measured by FLS980 spectrometer with the excitation light at 365 nm. The PLQY reached the highest value of 37.0% when doping concentration *x* was 0.59%. Further increase of the dopants caused the self-quenching effect, which is a typical character of ionoluminescence [33]. The ionoluminescence nature of this material will be discussed in the later part.

The Cs_2SnCl_6:0.59%Sb sample, with the highest PLQY of 37.0%, was selected as the representative sample for further exploration. Figure 2(a) shows the optical absorption spectra of Cs_2SnCl_6:0.59%Sb crystals which match reasonably well with the excitation spectra (Fig. 2(b)). In the optical absorption spectrum (Fig. S3) for series of Cs_2SnCl_6:*x*Sb crystals, we could clearly observe that the absorbance intensity increased with the increase of Sb content within the region of 300 – 400 nm. Thereby we attributed the absorption in this region to the Sb^{3+} induced ion absorption. As shown in Fig. 2(b), Cs_2SnCl_6:0.59%Sb exhibited a broad emission peak (FWHM > 100 nm) at 602 nm with a large Stokes shift of 237 nm. We suspected that the broad emission with large Stokes shift was due to that outermost S-P electron orbital transition of Sb^{3+} was highly sensitive to the distortion of Sb-Cl polyhedron and crystal field [24,34–36].

To figure out the mechanism of luminescence, herein we conducted the temperature dependent photoluminescence (TDPL) measurement for Cs_2SnCl_6:0.59%Sb (Fig. 3(a)) and clearly observed two emission peaks with the decreasing temperature. This emission character is a strong indicator of ionoluminescence.

As studied in many previous papers, for ions with the outer electronic configuration as s^2 (here is $5s^2$ for Sb^{3+}), the ground state of s^2 ion is $^1S_0$, whereas the excited state (sp) splits into four energy levels, namely $^1P_1$, $^3P_0$, $^3P_1$ and $^3P_2$ (Fig. 3(b)). According to the transition rule, $^1S_0$-$^1P_1$ transition is allowed and $^1S_0$-$^3P_1$ transition is partially allowed due to a spin-orbit coupling for heavy atoms, while $^1S_0$-$^3P_2$ and $^1S_0$-$^3P_0$ transitions are totally forbidden at the electric dipole transition level [35,37,38]. The photoluminescence within the visible light region is possibly from the transition of $^3P_1$-$^1S_0$ and also the double emission peaks at low temperature conforms to the asymmetric doublet characteristics for $^3P_1$-$^1S_0$ transition

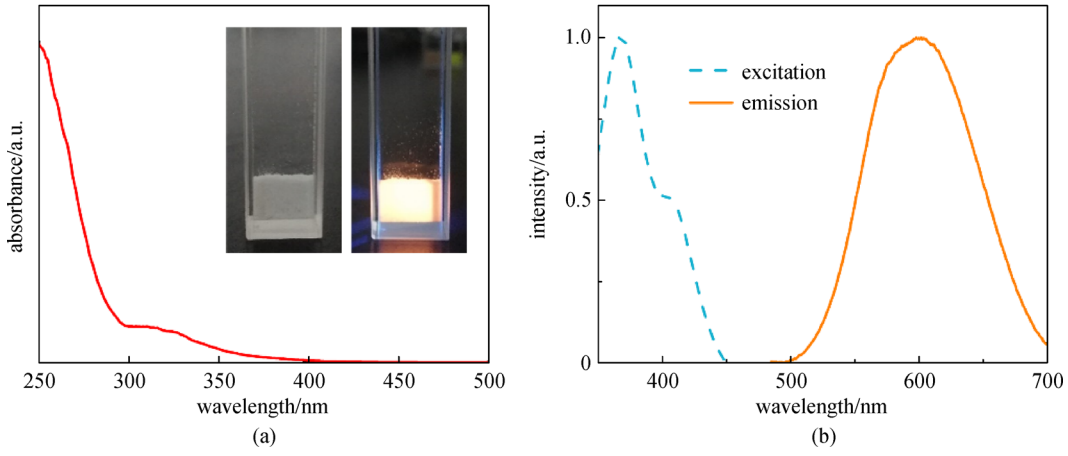

Fig. 2 (a) Optical absorption spectrum of Cs_2SnCl_6:0.59%Sb, the insets show the images of Cs_2SnCl_6:0.59%Sb under the natural light (left) and UV irradiation (right). (b) Excitation and photoluminescence spectra of Cs_2SnCl_6:0.59%Sb

Table 1 Photophysical properties of Cs_2SnCl_6:*x*Sb at room temperature (*x* is the content of antimony; λ_{ex} is the wavelength at the excitation maximum; λ_{em} is the wavelength at the emission maximum)

x	λ_{ex}/nm	λ_{em}/nm	FWHM/nm	Stokes shift/nm	PLQY
0	N/A	N/A	N/A	N/A	N/A
0.20%	365	601	101	236	25.9%
0.41%	364	601	102	237	28.3%
0.59%	365	602	101	237	37.0%
0.89%	365	604	102	239	32.0%
0.98%	366	602	100	236	21.9%

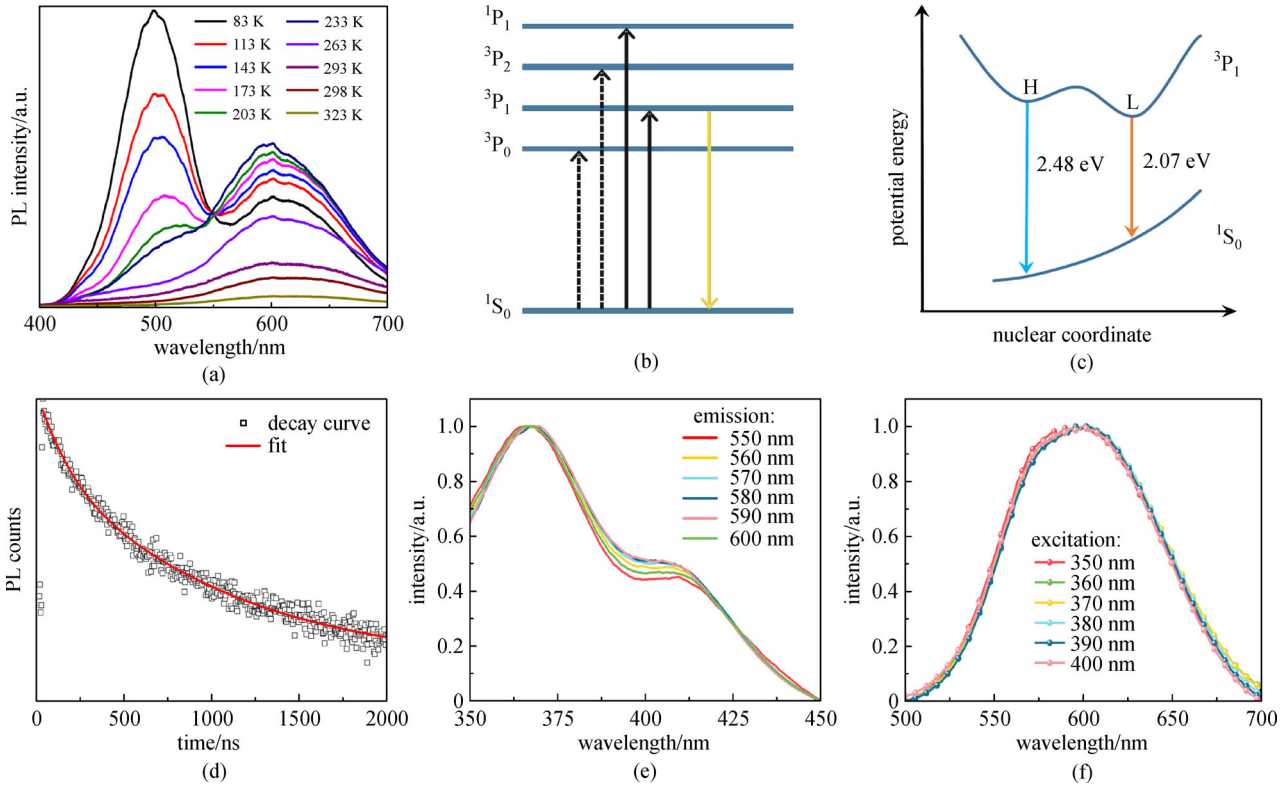

Fig. 3 (a) Temperature-dependent photoluminescence spectra of Cs_2SnCl_6:0.59%Sb. (b) Schematic diagram of luminescence process in Cs_2SnCl_6:*x*Sb. (c) Schematic of the potential energy curves of Cs_2SnCl_6:*x*Sb in a configuration space. (d) PL decay curve of Cs_2SnCl_6:0.59%Sb bulk crystals (λ_{ex} = 365 nm, λ_{em} = 602 nm). The red curve is a fit to the experimental data with a double exponential decay function. (e) Excitation spectra of PL monitored at different emission wavelengths. (f) Emission spectra of PL monitored at different excitation wavelengths

[38]. Several previous papers have documented that the transition of $^3P_1$-$^1S_0$ could be split into two transitions due to the Jahn-Teller effect of $^3P_1$ [35,38,39], and here the two derived transition bands are termed as H transition (2.48 eV) and L transition (2.07 eV) (i.e., the blue and orange lines in Fig. 3(c)). The intensity of these two transitions could be changed as we altered the measurement temperature. As shown in Fig. S4, the PL intensity based from H transition was much higher than L transition in the low-temperature region (83 – 143 K). Upon the temperature further increased, the PL intensity based from L transition became stronger than H transition due to the thermal population of the carrier from H transition band to L transition band. The same phenomenon has been observed in many ionoluminescence with ns^2 ions as the luminescent centers, such as Sb^{3+} doped phosphate/borax/germanate, In^+ doped KCl [36].

Unlike our previous work about Cs_2SnCl_6:Bi whose photoluminescence derived from defect band induced by Bi-doping [27], here Cs_2SnCl_6:Sb exhibited discrete ionoluminescence properties. We suspected the reason for this difference was that there was no continuous defect band formed since the excited state was strongly localized with the tiny content of antimony.

In addition, the photoluminescence decay behavior of the activator in host materials is significant to gain more insight into the luminescence mechanism. Figure 3(d) shows the time-resolved PL decay curve of Cs_2SnCl_6:0.59% Sb measured at 600 nm excited by 365 nm light at room temperature. The curve can be fitted well by the following biexponential fitting (Eq. (1)):

$$A(t) = A_1\exp(-t/\tau_1) + A_2\exp(-t/\tau_2), \qquad (1)$$

where $A(t)$ is the time variation of PL intensity at time t, A_1 and A_2 are the initial PL intensity of two component, and τ_i (i = 1,2) represents the decay time of i component.

Accordingly, we obtained a short-lived PL lifetime of 153.8 ns with a percentage of 39.9% and a long-lived PL lifetime of 821.2 ns with a percentage of 60.1%. According to previous study [36], the excited state of $^3P_1$ for Sb^{3+} has two recombination route, i.e., $^3P_1$-$^3P_0$ transition within the excited state with a fast decay rate and $^3P_1$-$^1S_0$ radiative recombination with a slow decay rate. Thereby we could attribute the observed two decay lifetimes of Cs_2SnCl_6:0.59% to $^3P_1$-$^3P_0$ and $^3P_1$-$^1S_0$ transitions.

For the representative Cs_2SnCl_6:0.59%Sb sample, when the monitored emission wavelength was varied from 550 to 600 nm, the corresponding excitation spectra (Fig. 3(e)) show negligible peak shift or shape change. Similarly, when the excited wavelength varied from 350 to 400 nm,

the corresponding emission spectra (Fig. 3(f)) show negligible changes as well. These negligible changes conformed to the characteristics of ionoluminescence, and verified that the photoluminescence was not derived from Raman scattering or defects.

It is also notable that the synthesized Cs_2SnCl_6:*x*Sb samples exhibit good stability. In Fig. 4(a), thermogravimetric analysis (TGA) and differential scanning calorimetry (DSC) shows that the Cs_2SnCl_6:0.59%Sb sample melt around 396°C and decomposed at 606°C. This decomposition temperature is much higher than organic-inorganic hybrid perovskite ABX_3 (A = CH_3NH_3, $HC(NH_2)_2$; B = Pb, Sn; X = Cl, Br, I) [23,40]. We further utilized 365 nm UV light (UVLS-26, 1200 uW at a distance of three inches) to irradiate Cs_2SnCl_6:0.59%Sb sample for 24 h and observed little PL decay (Fig. 4(b)). Such observation indicated that Cs_2SnCl_6:Sb had excellent photo-stability due to its all-inorganic structure. Unlike conventional lead halide perovskite $CsPbBr_3$ and antimony-based metal halide hybrids (like $Cs_3Sb_2Br_9$, $(C_9NH_{20})_2SbCl_5$ and $(Ph_4P)_2SbCl_5$), Cs_2SnCl_6:0.59%Sb retained its luminescence after 120 min soaking in water (Fig. S5). In addition, Cs_2SnCl_6:0.59%Sb exhibited no degradation within storage in air for two months, demonstrating its good air stability (Fig. S6). Figure 4(c) shows that Cs_2SnCl_6:0.59% Sb retained 92% of the original PL intensity after immersing in deionized water for 24 h. We suspected that this good water-stability possibly derived from the presence of SbOCl on the surface (see Figs. S2 and S7 in the Supporting Information) and the inherently low solubility of Cs_2SnCl_6 in water, similar to our previous Cs_2SnCl_6:*x*Bi phosphor.

The high stability and large Stokes shift endow the all-inorganic lead-free Cs_2SnCl_6:*x*Sb material with highly promising prospects in a variety of applications like lighting, fluorescence imaging technique and so on. To demonstrate the application of lighting, we fabricated a commercial UV chip (380 nm) pumped cold white-LED by mixing Cs_2SnCl_6:0.59%Sb with our home-made blue phosphor Cs_2SnCl_6:2.75%Bi and green phosphor $Ba_2Sr_2SiO_4:Eu^{2+}$ into the silicone. The ratio between each phosphor is optimized to obtain the best white emission.

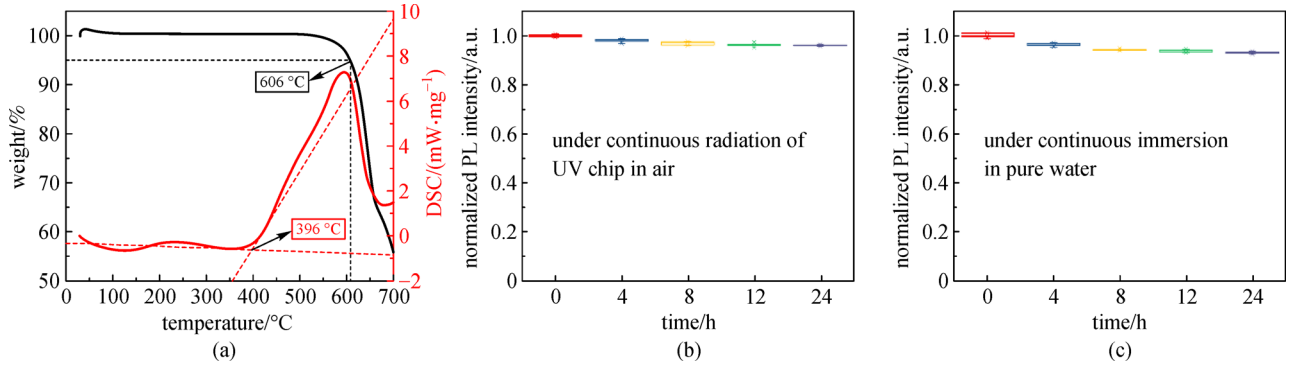

Fig. 4 (a) TGA and DSC of Cs_2SnCl_6:0.59%Sb. (b) PL stability of Cs_2SnCl_6:0.59%Sb by illuminating with UV light (365 nm). The measurements were conducted in air without any encapsulation. (c) PL stability of Cs_2SnCl_6:0.59%Sb after immersed into deionized water for different durations

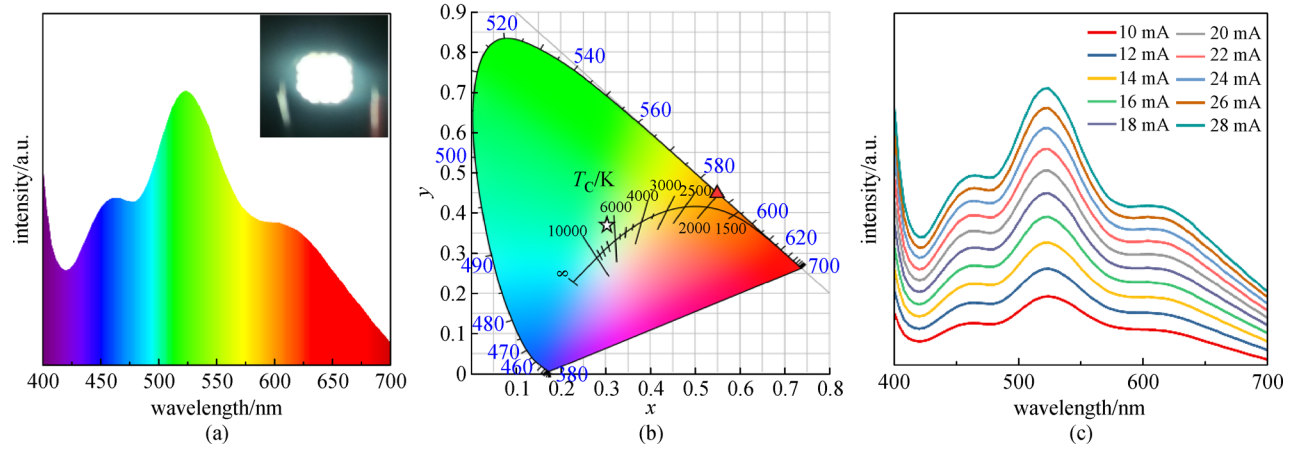

Fig. 5 (a) Luminescence spectra from Cs_2SnCl_6:0.59%Sb-based LEDs with cold white emission and (inset) photo of an operating LED. (b) CIE coordinates and CCTs corresponding to white-LED device (white star) and Cs_2SnCl_6:0.59%Sb crystals (red triangle). (c) Emission spectra of white-LED device at different driving currents

Figure 5(a) shows the emission spectra and the image of the working white-LED. Figure 5(b) shows the Commission Internationale de L'Eclairage (CIE) coordinates of Cs_2SnCl_6:0.59%Sb phosphor and our white-LED. For the orange emission of Cs_2SnCl_6:0.59%Sb, it reveals a CIE color coordinate of (0.55, 0.45) and correlated color temperature (CCT) of 2087 K. With a blue/green/orange ratio of 1:1:1, a cold white-LED with CIE color coordinate of (0.30, 0.37), CCT of 6815 K and the CRI of 81, was obtained. The white-LED exhibited excellent color stability at different operating currents (Fig. 5(c)), as well as under various operating times (Fig. S8), which was ascribed to the negligible energy transfer among different phosphors and the great stability respectively. These excellent performances enable the Cs_2SnCl_6:*x*Sb to be a promising candidate for lighting phosphor.

4 Conclusion

In summary, we have designed and synthesized a Cs_2SnCl_6:*x*Sb phosphor with orange-red emission and photoluminescence quantum efficiency of ~37%, as well as good stability against both water and heat. This material has a photoluminescence emission at 602 nm and a large FWHM of 101 nm, which precisely matches our previous blue perovskite for lighting application. The temperature dependent PL and PL decay verify the ionoluminescence of Sb^{3+} within Cs_2SnCl_6 matrix. Finally, a cold white-LED with a high CRI of 81 was fabricated by mixing this material with our previously synthesized blue phosphor Cs_2SnCl_6:Bi and commercial green phosphor.

Acknowledgements This work was financially supported by the National Natural Science Foundation of China (Grant Nos. 51761145048, 61725401 and 51702107), the National Key R&D Program of China (No. 2016YFB0700702) and the China Postdoctoral Science Foundation (No. 2018M632843). The authors thank the Analytical and Testing Center of HUST and the facility support of the Center for Nanoscale Characterization and Devices, WNLO. The work at Tokyo Institute of Technology was conducted under the Tokodai Institute for Element Strategy (TIES) funded by the MEXT Elements Strategy Initiative to Form Core Research Center.

References

1. Burschka J, Pellet N, Moon S J, Humphry-Baker R, Gao P, Nazeeruddin M K, Grätzel M. Sequential deposition as a route to high-performance perovskite-sensitized solar cells. Nature, 2013, 499(7458): 316–319
2. Zhang L, Yang X, Jiang Q, Wang P, Yin Z, Zhang X, Tan H, Yang Y M, Wei M, Sutherland B R, Sargent E H, You J. Ultra-bright and highly efficient inorganic based perovskite light-emitting diodes. Nature Communications, 2017, 8: 15640
3. Cho H, Jeong S H, Park M H, Kim Y H, Wolf C, Lee C L, Heo J H, Sadhanala A, Myoung N, Yoo S, Im S H, Friend R H, Lee T W. Overcoming the electroluminescence efficiency limitations of perovskite light-emitting diodes. Science, 2015, 350(6265): 1222–1225
4. Tan Z K, Moghaddam R S, Lai M L, Docampo P, Higler R, Deschler F, Price M, Sadhanala A, Pazos L M, Credgington D, Hanusch F, Bein T, Snaith H J, Friend R H. Bright light-emitting diodes based on organometal halide perovskite. Nature Nanotechnology, 2014, 9 (9): 687–692
5. Li X, Wu Y, Zhang S, Cai B, Gu Y, Song J, Zeng H. $CsPbX_3$ quantum dots for lighting and displays: room-temperature synthesis, photoluminescence superiorities, underlying origins and white light-emitting diodes. Advanced Functional Materials, 2016, 26(15): 2584
6. Zhang H, Wang X, Liao Q, Xu Z, Li H, Zheng L, Fu H. Embedding perovskite nanocrystals into a polymer matrix for tunable luminescence probes in cell imaging. Advanced Functional Materials, 2017, 27(7): 1604382
7. Ge R, Qin F, Hu L, Xiong S, Zhou Y. High fill factor over 82% enabled by a biguanide doping electron transporting layer in planar perovskite solar cells. Frontiers of Optoelectronics, 2018, 11(4): 360–366
8. Lin K, Xing J, Quan L N, de Arquer F P G, Gong X, Lu J, Xie L, Zhao W, Zhang D, Yan C, Li W, Liu X, Lu Y, Kirman J, Sargent E H, Xiong Q, Wei Z. Perovskite light-emitting diodes with external quantum efficiency exceeding 20 percent. Nature, 2018, 562(7726): 245–248
9. Cao Y, Wang N, Tian H, Guo J, Wei Y, Chen H, Miao Y, Zou W, Pan K, He Y, Cao H, Ke Y, Xu M, Wang Y, Yang M, Du K, Fu Z, Kong D, Dai D, Jin Y, Li G, Li H, Peng Q, Wang J, Huang W. Perovskite light-emitting diodes based on spontaneously formed submicrometre-scale structures. Nature, 2018, 562(7726): 249–253
10. Veldhuis S A, Boix P P, Yantara N, Li M, Sum T C, Mathews N, Mhaisalkar S G. Perovskite materials for light-emitting diodes and lasers. Advanced Materials, 2016, 28(32): 6804–6834
11. Lignos I, Stavrakis S, Nedelcu G, Protesescu L, deMello A J, Kovalenko M V. Synthesis of cesium lead halide perovskite nanocrystals in a droplet-based microfluidic platform: fast parametric space mapping. Nano Letters, 2016, 16(3): 1869–1877
12. Song J, Li J, Xu L, Li J, Zhang F, Han B, Shan Q, Zeng H. Room-temperature triple-ligand surface engineering synergistically boosts ink stability, recombination dynamics, and charge injection toward EQE-11.6% perovskite QLEDs. Advanced Materials, 2018, 30(30): e1800764
13. Protesescu L, Yakunin S, Bodnarchuk M I, Krieg F, Caputo R, Hendon C H, Yang R X, Walsh A, Kovalenko M V. Nanocrystals of cesium lead halide perovskites ($CsPbX_3$, X = Cl, Br, and I): novel optoelectronic materials showing bright emission with wide color gamut. Nano Letters, 2015, 15(6): 3692–3696
14. Zhang F, Zhong H, Chen C, Wu X G, Hu X, Huang H, Han J, Zou B, Dong Y. Brightly luminescent and color-tunable colloidal $CH_3NH_3PbX_3$ (X = Br, I, Cl) quantum dots: potential alternatives for display technology. ACS Nano, 2015, 9(4): 4533–4542
15. Pan W, Wu H, Luo J, Deng Z, Ge C, Chen C, Jiang X, Yin W, Niu G, Zhu L, Yin L, Zhou Y, Xie Q, Ke X, Sui M, Tang J. $Cs_2AgBiBr_6$ single-crystal X-ray detectors with a low detection limit. Nature

Photonics, 2017, 11(11): 726–732
16. Wei Y, Xiao H, Xie Z, Liang S, Liang S, Cai X, Huang S, Al Kheraif A A, Jang H S, Cheng Z, Lin J. Highly luminescent lead halide perovskite quantum dots in hierarchical CaF_2 matrices with enhanced stability as phosphors for white light-emitting diodes. Advanced Optical Materials, 2018, 6(11): 1701343
17. Huang S, Wang B, Zhang Q, Li Z, Shan A, Li L. Postsynthesis potassium-modification method to improve stability of $CsPbBr_3$ perovskite nanocrystals. Advanced Optical Materials, 2018, 6(6): 1701106
18. Yang S, Fu W, Zhang Z, Chen H, Li C. Recent advances in perovskite solar cells: efficiency, stability and lead-free perovskite. Journal of Materials Chemistry A, Materials for Energy and Sustainability, 2017, 5(23): 11462–11482
19. Leng M, Chen Z, Yang Y, Li Z, Zeng K, Li K, Niu G, He Y, Zhou Q, Tang J. Lead-free, blue emitting bismuth halide perovskite quantum dots. Angewandte Chemie, 2016, 55(48): 15012–15016
20. Zhang J, Yang Y, Deng H, Farooq U, Yang X, Khan J, Tang J, Song H. High quantum yield blue emission from lead-free inorganic antimony halide perovskite colloidal quantum dots. ACS Nano, 2017, 11(9): 9294–9302
21. Leng M, Yang Y, Zeng K, Chen Z, Tan Z, Li S, Li J, Xu B, Li D, Hautzinger M P, Fu Y, Zhai T, Xu L, Niu G, Jin S, Tang J. All-inorganic bismuth-based perovskite quantum dots with bright blue photoluminescence and excellent stability. Advanced Functional Materials, 2018, 28(1): 1704446
22. Leng M, Yang Y, Chen Z, Gao W, Zhang J, Niu G, Li D, Song H, Zhang J, Jin S, Tang J. Surface passivation of bismuth-based perovskite variant quantum dots to achieve efficient blue emission. Nano Letters, 2018, 18(9): 6076–6083
23. Zhou C, Lin H, Tian Y, Yuan Z, Clark R, Chen B, van de Burgt L J, Wang J C, Zhou Y, Hanson K, Meisner Q J, Neu J, Besara T, Siegrist T, Lambers E, Djurovich P, Ma B. Luminescent zero-dimensional organic metal halide hybrids with near-unity quantum efficiency. Chemical Science, 2018, 9(3): 586–593
24. Zhou C, Worku M, Neu J, Lin H, Tian Y, Lee S, Zhou Y, Han D, Chen S, Hao A, Djurovich P I, Siegrist T, Du M H, Ma B. Facile preparation of light emitting organic metal halide crystals with near-unity quantum efficiency. Chemistry of Materials, 2018, 30(7): 2374–2378
25. Liu W, Lin Q, Li H, Wu K, Robel I, Pietryga J M, Klimov V I. Mn^{2+}-doped lead halide perovskite nanocrystals with dual-color emission controlled by halide content. Journal of the American Chemical Society, 2016, 138(45): 14954–14961
26. Hu Q, Li Z, Tan Z, Song H, Ge C, Niu G, Han J, Tang J. Rare earth ion-doped $CsPbBr_3$ nanocrystals. Advanced Optical Materials, 2018, 6(2): 1700864
27. Zhou C, Tian Y, Khabou O, Worku M, Zhou Y, Hurley J, Lin H, Ma B. Manganese-doped one-dimensional organic lead bromide perovskites with bright white emissions. ACS Applied Materials & Interfaces, 2017, 9(46): 40446–40451
28. Tan Z, Li J, Zhang C, Li Z, Hu Q, Xiao Z, Kamiya T, Hosono H, Niu G, Lifshitz E, Cheng Y, Tang J. Highly efficient blue-emitting Bi-doped Cs_2SnCl_6 perovskite variant: photoluminescence induced by impurity doping. Advanced Functional Materials, 2018, 28(29): 1801131
29. Costa D, Marcus P. Electronic core levels of hydroxyls at the surface of chromia related to their XPS O 1s signature: a DFT + U study. Surface Science, 2010, 604(11–12): 932–938
30. Hwang S M, Kim J, Kim Y, Kim Y. Na-ion storage performance of amorphous Sb_2S_3 nanoparticles: anode for Na-ion batteries and seawater flow batteries. Journal of Materials Chemistry A, Materials for Energy and Sustainability, 2016, 4(46): 17946–17951
31. Yang X, Ma J, Wang H, Chai Y, Yuan R. Partially reduced Sb/Sb_2O_3@C spheres with enhanced electrochemical performance for lithium ion storage. Materials Chemistry and Physics, 2018, 213: 208–212
32. Ali A, Hasanain S K, Ali T, Sultan M. Improvement of antimony sulfide photo bsorber performance by interface modification in Sb_2S_3-ZnO hybrid nanostructures. Physica E, Low-Dimensional Systems and Nanostructures, 2017, 87: 20–26
33. Yang P, Deng P, Yin Z. Concentration quenching in Yb:YAG. Journal of Luminescence, 2002, 97(1): 51–54
34. Oomen E W J L, Dirksen G J, Smit W M A, Blasse G. On the luminescence of the Sb^{3+} ion in Cs_2NaMBr_6 (M = Sc,Y,La). Journal of Physics C, Solid State Physics, 1987, 20(8): 1161–1171
35. Oomen E W J L, Smit W M A, Blasse G. On the luminescence of Sb^{3+} in Cs_2NaMCl_6 (with M = Sc,Y,La): a model system for the study of trivalent s^2 ions. Journal of Physics C, Solid State Physics, 1986, 19(17): 3263–3272
36. Reisfeld R, Boehm L, Barnett B. Luminescence and nonradiative relaxation of Pb^{2+}, Sn^{2+}, Sb^{3+}, and Bi^{3+} in oxide glasses. Journal of Solid State Chemistry, 1975, 15(2): 140–150
37. Zhou G, Jiang X, Zhao J, Molokeev M, Lin Z, Liu Q, Xia Z. Two-dimensional-layered perovskite $ALaTa_2O_7$:Bi^{3+} (A = K and Na) phosphors with versatile structures and tunable photoluminescence. ACS Applied Materials & Interfaces, 2018, 10(29): 24648–24655
38. Oomen E W J L, Dirksen G J. Crystal growth and luminescence of Sb^{3+}-doped Cs_2 $NaMCl_6$ (M = Sc, Y, La). Materials Research Bulletin, 1985, 20(4): 453–457
39. Blasse G, Grabmaier B. Luminescent Materials. Berlin: Springer, 1994
40. Kulbak M, Gupta S, Kedem N, Levine I, Bendikov T, Hodes G, Cahen D. Cesium enhances long-term stability of lead bromide perovskite-based solar cells. Journal of Physical Chemistry Letters, 2016, 7(1): 167–172

Jinghui Li received his B.S. degree from School of Materials Science and Engineering, Huazhong University of Science and Technology (HUST) China in 2017. He is currently a Ph.D. candidate in Prof. Jiang Tang's group in Wuhan National Laboratory for Optoelectronics (WNLO) at HUST. His current researches focus on luminescent perovskite materials and its application.

E-mail: kinghoy_li@163.com

Zhifang Tan received his Master's degree from Huazhong Normal University at 2010, and his Ph.D. degree in Applied Chemistry from Hiroshima University at 2014. Now he works toward Postdoctor in WNLO. His research interest includes the research and exploration of photoelectric materials, lead or lead-free perovskite materials.

Email: tanzhifang1985@163.com

Manchen Hu is a third-year undergraduate in School of Optical and Electronic Information, Huazhong University of Science and Technology (HUST). He joined Prof. Tang's research group in 2017. His research mainly focuses on novel materials and their applications in optoelectronic devices.

E-mail: manchenhu618@gmail.com

Guangda Niu is an associate professor at Wuhan National Laboratory for Optoelectronics, Huazhong University of Science and Technology, Wuhan, China. He is working on synthesis of metal halide perovskite semiconductors and their applications in optoelectronic devices.

E-mail: guangda_niu@hust.edu.cn

Jiang Tang received his Bachelor's degree from University of Science and Technology at 2003, and his Ph.D. degree in Material Science and Engineering from University of Toronto at 2010. He spent one year and half as a postdoctoral researcher at IBM T. J. Watson research center and then joined in Wuhan National Laboratory for Optoelectronics, Huazhong University of Science and Technology as a professor in 2012. His group focuses on antimony selenide (Sb_2Se_3) thin film solar cells, halide perovskites nanocrystals for light emitting and single crystals for X-ray detection. He has published 70 + papers including *Nature*, *Nat. Mater.*, *Nat. Energy* and *Nat. Photonics* with 3500 citations. He is the receiver of the "1000 Young Talents" and the National Natural Science Funds for Distinguished Young Scholar.

E-mail: jtang@mail.hust.edu.cn

Supporting Information

Table S1 Feeding concentrations and ICP-OES-determined concentrations of Sb/(Sb + Sn)

feeding concentrations	ICP-OES-determined concentrations
0.99%	0.20%
4.76%	0.41%
9.09%	0.59%
16.66%	0.89%
23.08%	0.98%

Table S2 Refined lattice parameters of Cs_2SnCl_6:*x*Sb, *x* represents the Sb/(Sb + Sn) molar ratio determined by ICP-OES

x	*a*/Å	R_p/%	R_{wp}/%	χ^2
0	10.37371	4.91	6.95	4.63
0.20%	10.37373	5.31	8.09	6.55
0.41%	10.38144	5.26	8.00	6.27
0.59%	10.38175	4.51	6.51	4.10
0.89%	10.38232	4.77	6.97	4.75
0.98%	10.38246	4.78	6.79	4.53

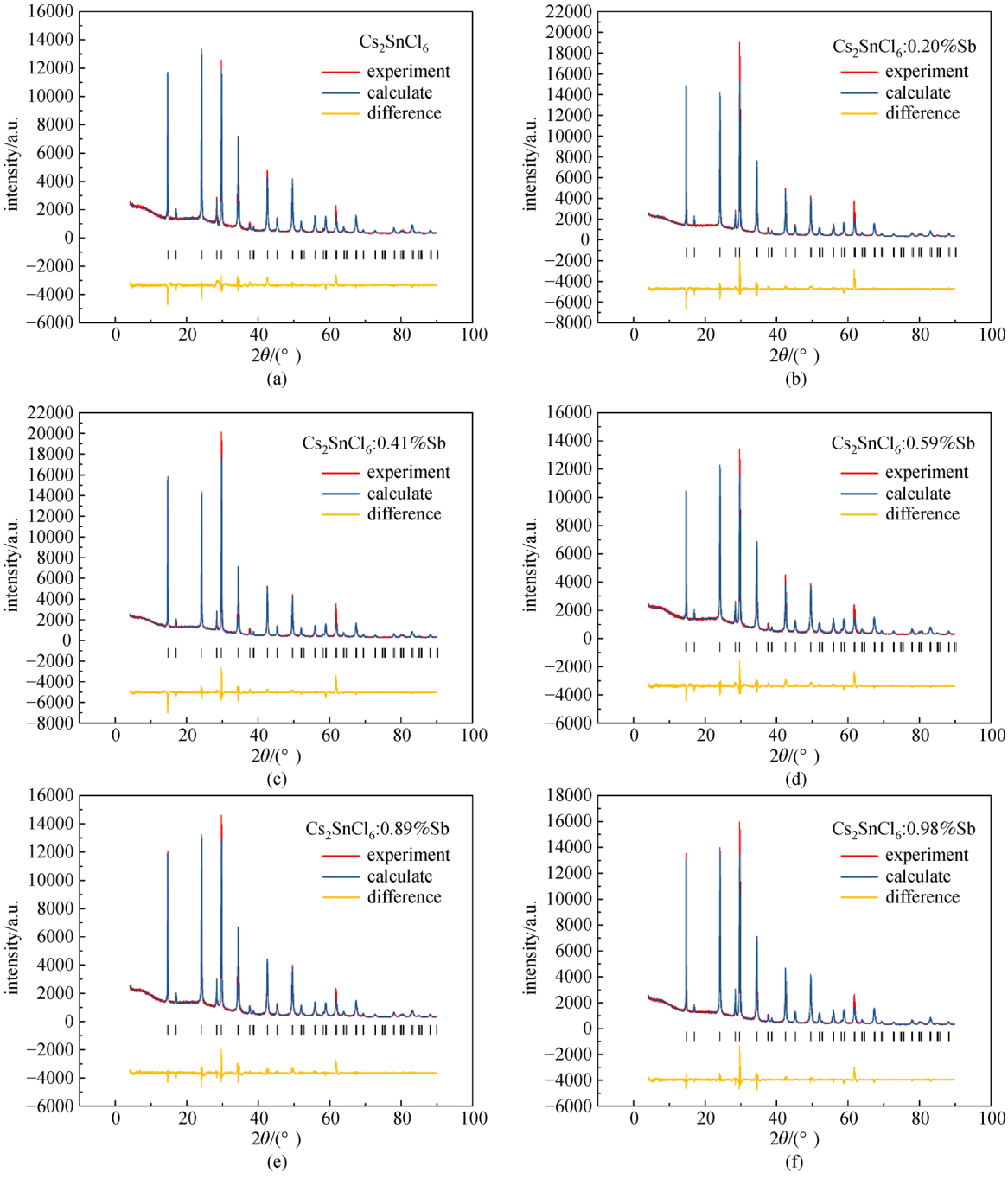

Fig. S1 High-resolution X-ray diffraction analysis and Rietveld refinements of Sb-doped Cs_2SnCl_6 with different content of antimony. The structural parameters and refinement statistics were included in Table S1

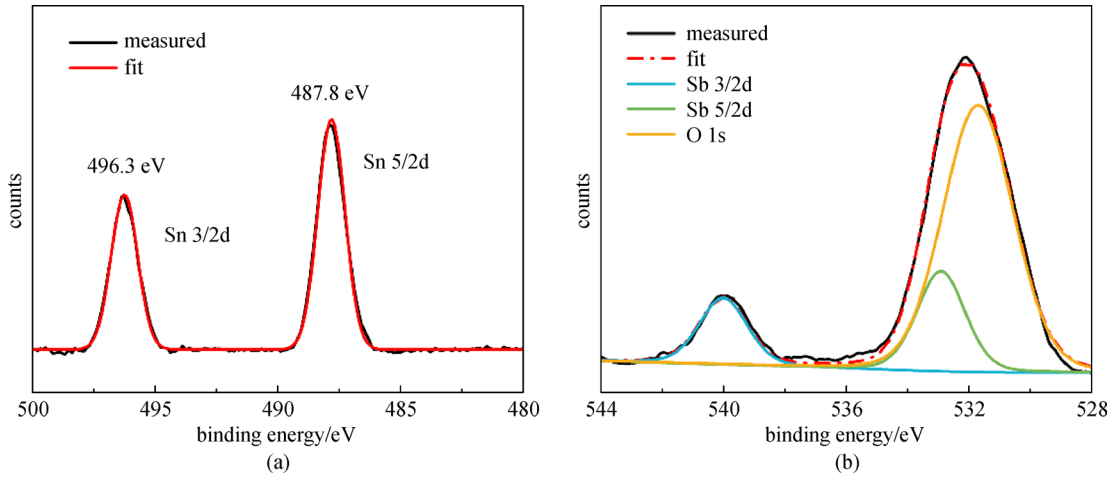

Fig. S2 High-resolution XPS spectra of Cs_2SnCl_6:0.59%Sb and peak fitting for (a) Sn^{4+} and (b) Sb^{3+}, respectively

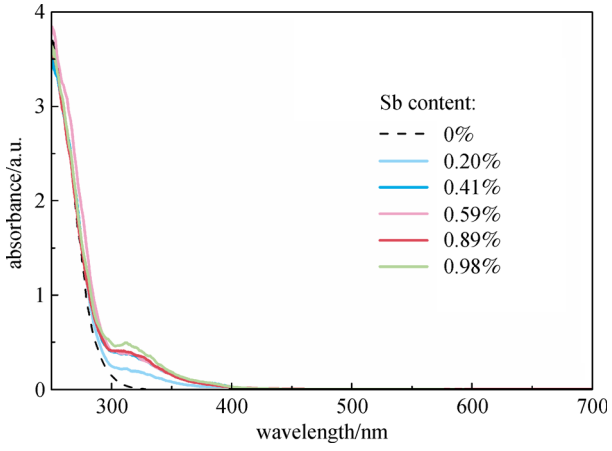

Fig. S3 Optical absorption spectra of Sb-doped Cs_2SnCl_6

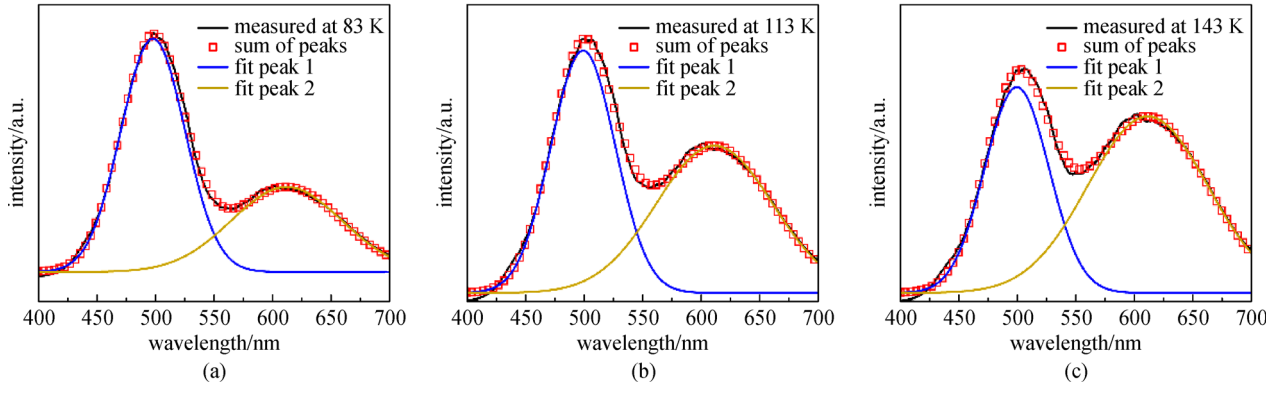

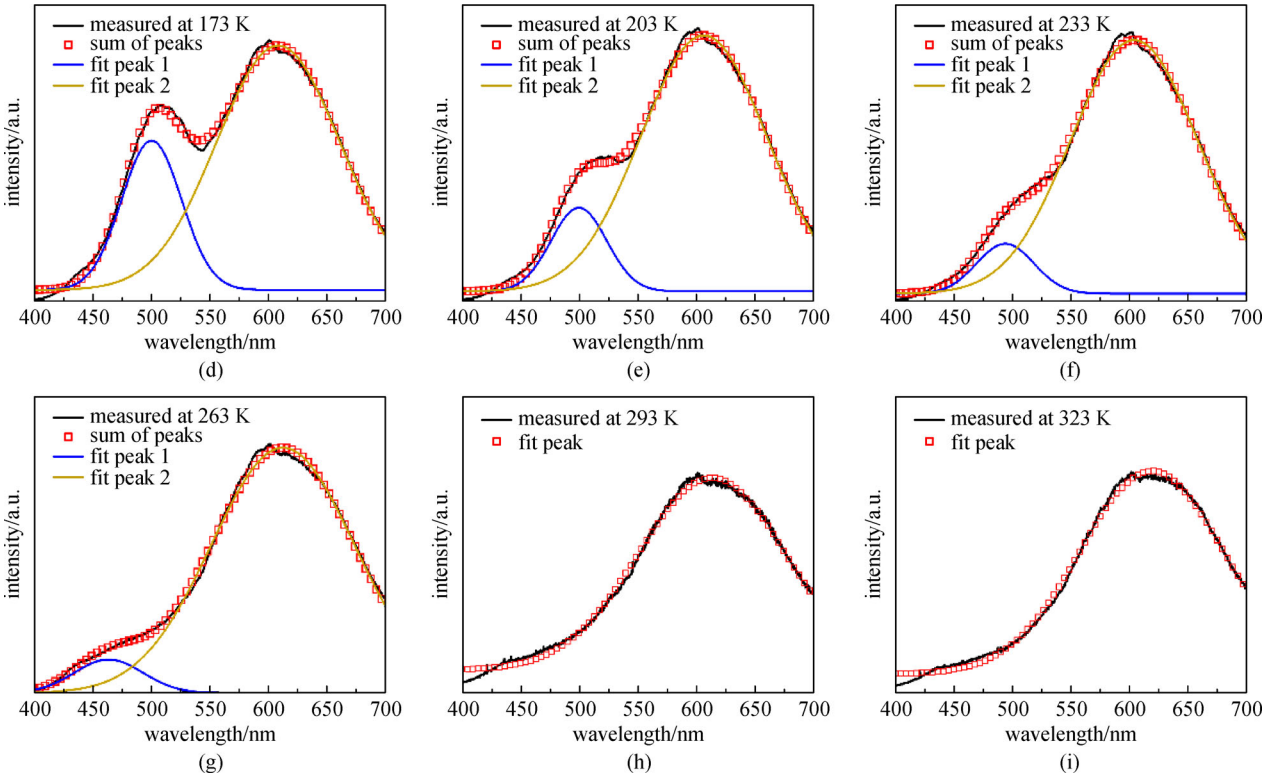

Fig. S4 Temperature-dependent photoluminescence spectra and the corresponding Gaussian fitting results

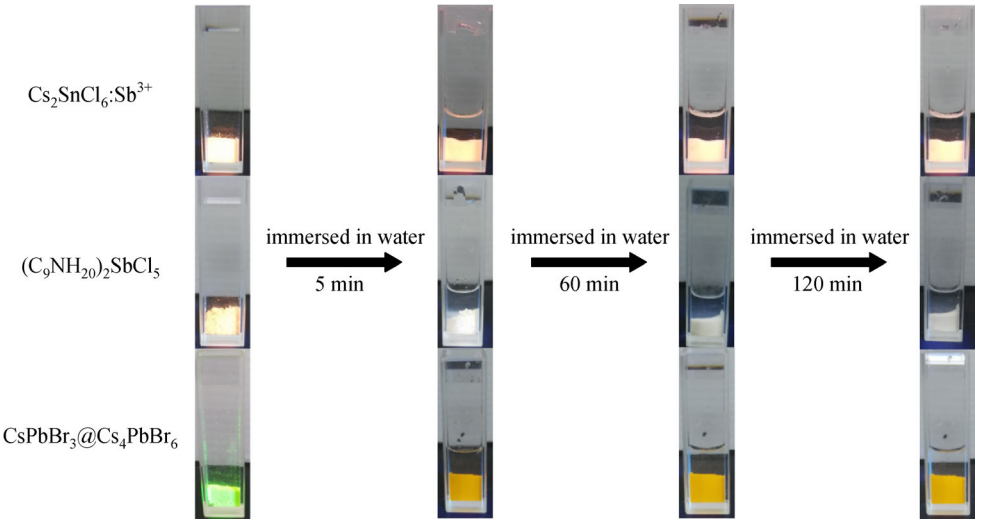

Fig. S5 Anti-water stability comparison among $Cs_2SnCl_6:Sb^{3+}$, $(C_9NH_{20})_2SbCl_5$ and $CsPbBr_3@Cs_4PbBr_6$ (i.e., the core-shell structure of $CsPbBr_3$-Cs_4PbBr_6). The latter two samples are reproduced from literature by ourselves

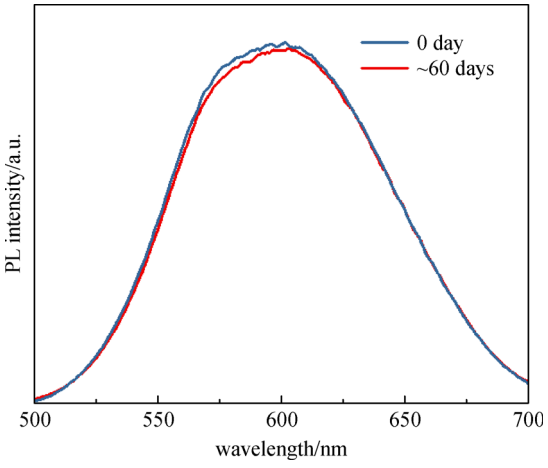

Fig. S6 Air stability of Pb-free perovskites Cs_2SnCl_6:0.59%Sb

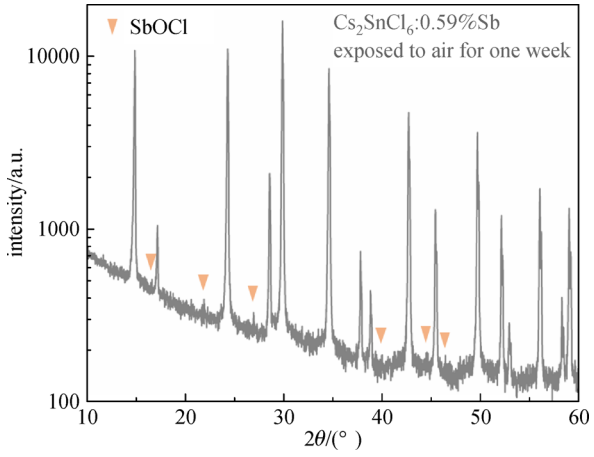

Fig. S7 XRD pattern for Cs_2SnCl_6:0.59%Sb^{3+} sample after exposed to air for one week. The inverted triangles marks represent the X-Ray Diffraction peaks for SbOCl

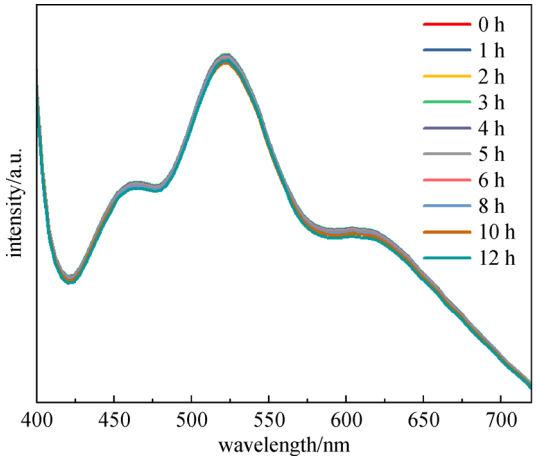

Fig. S8 Operational LED stability of Pb-free perovskites Cs_2SnCl_6:*x*Sb